Supporting Information

Low-Overpotential Electroreduction of Carbon Monoxide Using Copper Nanowires

David Raciti,[1,†] Liang Cao,[2,3,†] Kenneth J. T. Livi,[3] Paul F. Rottmann,[3,4] Xin Tang[5], Chenyang Li,[3] Zachary Hicks[5], Kit H. Bowen,[5] Kevin J. Hemker,[4] Tim Mueller,[3,*] Chao Wang[1,*]

[1]Department of Chemical and Biomolecular Engineering, [2] Department of Physics and Astronomy, [3]Department of Materials Science and Engineering, [4]Department of Mechanical Engineering and [5]Department of Chemistry, Johns Hopkins University, Baltimore, Maryland 21218

[†]Equal contribution.

[*]Email: tmueller@jhu.edu; chaowang@jhu.edu.

S1. Experimental Methods

Materials. KOH Pellets (99.99% trace metals basis) were purchased from Sigma-Aldrich; $HClO_4$ (69-72%) was purchased from VWR International; copper mesh (100 mesh) was purchased from McMaster-Carr. All materials were used without further purification unless otherwise noted. Electrolyte solutions were prepared using 18.2 MΩ H2O (Elga Veolia).

Synthesis of CuO Nanowires. Cu mesh was cut to a desired size and then sonicated for 1 minute in 0.1 M $HClO_4$. The sample was then thoroughly rinsed in deionized H_2O. The cleaned Cu mesh was dried in vacuum and placed into an oven pre-set to 600 °C.[1] After annealing in air for 8 hours, the Cu mesh turned from red to black, indicating the formation of copper oxide nanowires. The mesh was then subjected to reduction by hydrogen using forming gas (5% H_2/N_2) at various temperatures: 150 °C (15 h), 200 °C (1 h), and 300 °C (1 or 15 h) to form Cu nanowires.

Material Characterization. SEM images were collected on a JEOL JSM-6700F field-emission scanning electron microscope. A field-emission Phillips CM300-FEG (300 kV) was used for TEM imaging and collecting the electron diffraction patterns for crystalline structure and grain boundary analysis. The density of grain boundaries is determined statistically as the average lengths of grain boundaries per area of the nanowires (nm^{-1}). X-ray diffraction (XRD) patterns were collected on a PANalytical X'Pert3 Powder X-ray diffractometer equipped with a Cu Kα source (λ=0.15406).

Electrocatalysis. The electrocatalytic activities of the Cu nanowire catalysts were measured using a gas-tight electrolysis cell and an Autolab 302 potentiostat (Metrohm). A Hg/HgO electrode (Koslow Scientific) and a Pt mesh (VWR) were used as the reference and counter electrode, respectively. A solution of 0.1 M KOH was used as the electrolyte (the pH value was measured to be 13 under CO saturation). CO was delivered to the cathode compartment at a constant rate of 5 sccm and was allowed to purge for 30 minutes prior to the measurements. The cathode and anode compartments were separated with an anion exchange membrane (Selemion Inc.). All the catalytic results presented in the main text are the average of the

measurements over a duration of 1 hour and reported versus the reversible hydrogen electrode (RHE) with iR drop correction.

Gas- and liquid-phase products were analyzed by using GC-MS and NMR, respectively. A small amount of acetate was detected in the counter electrode compartment for catalysts that produced acetate as a significant product. This was probably due to the migration of acetate across the anion exchange membrane. The concentration was found to be <10% of that from the cathode side at the highest yield of acetate, namely at −0.25 V for the HR-150 Cu nanowires. This amount of acetate was not included in the reported FEs for acetate.

Cyclic voltammograms (CVs) were recorded between 0 and 0.4 V (vs. Ag/AgCl) at various scan rates in the electrolysis cell with 0.1 M $KClO_4$ as the electrolyte (purged with Ar). The capacitance was determined by evaluating the slope of the double layer vs scan rate (Figure S3). Electrochemically active surface areas (ECSAs) were estimated by comparing the capacitance measured on the Cu mesh with Cu nanowires to that reported for polycrystalline Cu electrodes[2] (Table S1). The specific current density (current normalized by the ECSA) are denoted as mA/cm^2_{Cu} (Figure S4).

Electrosorption of Hydroxide (OH_{ad}). CVs for OH_{ad} analysis were recorded in the electrolysis cell using Ar purged 1 M KOH as the electrolyte. In attempts to minimize bulk oxidation of Cu, a potential window from -0.2 to 0.55 V (vs. RHE) was selected. Droog and Schlenter reported that electrosorption of hydroxide on Cu bulk electrodes occurs prior to 0.55 V and distinctive OH_{ad} peaks are associated with various types of low-index Cu single-crystal surface (Figure S12).[3] By referring to the results reported for the Cu single crystals, the peaks exhibited in the CVs (between ca. 0.3 – 0.5 V) of Cu nanowires can be assigned to (111), (110) and (100) facets of Cu (Figure S13 and S14).[1] An additional peak at lower potentials is tentatively assigned to stepped surfaces such as (211) and defect sites such as adatoms and adislands that have smaller coordination numbers, which is denoted as (211)* in the discussion.

CO-TPD. Patterns for temperature-programmed desorption of CO (CO-TPD) were

collected in a UHV chamber (~10^{-9} Torr). The Cu meshes with Cu nanowires were mounted onto two crossed tungsten wires. The samples were cooled by using liquid nitrogen and heated by passing DC current through the tungsten wires, and the temperature was measured by a K-type thermocouple attached to the back of the sample. Before a TPD experiment, the sample was pre-annealed with 2*10^{-7} torr CO at 150°C for 1 hour. 1 Langmuir of isotopically labeled ^{13}CO was dosed via leak valve at 120 K. After that, the sample temperature was raised with a ramping rate of 3 K/s, and meanwhile the desorption of ^{13}CO was monitored by Hiden 3F/PIC quadrupole mass spectrometer at 29 amu.

CO-TPD plots were fitted using Lorentzian-Gaussian functions. CO binding energies were obtained by using the Redhead Formula,

$$\Delta E_{des} = RT_{\max}\left[\ln\frac{v_1 \times T_{\max}}{\beta} - \ln\frac{\Delta E_{des}}{RT_{\max}}\right] . \quad (1)$$

To do this we make the assumption that the frequency factor, v_1, is assumed to be 10^{13} s^{-1}. The heat rate, β, was 3 K/s. The second term, $\ln\frac{\Delta E_{des}}{RT_{\max}}$, is smaller than the first term and can be assumed to be 3.64 with the error being about 1.5% for $10^8 < \frac{v_1}{\beta} < 10^{13}$ K^{-1}.[4] The peak positions were determined using the experimental values generated by Vollmer et al. on single-crystal Cu surfaces.[5] The area percentages of each peak are presented in the main text (Figure 3c).

S2. Supplemental Results

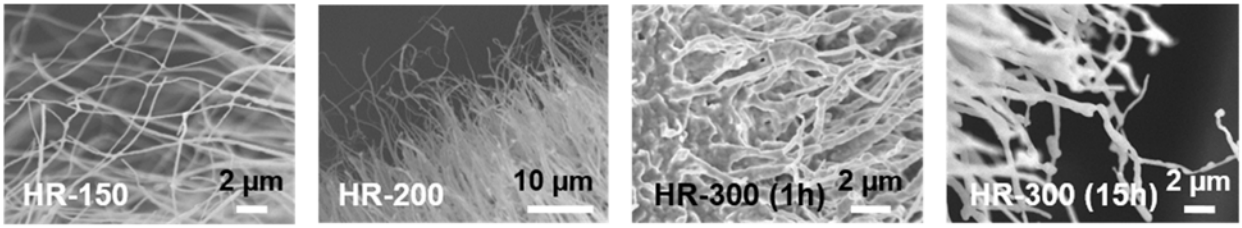

Figure S1. Cu nanowires produced by reduction of CuO nanowires. The Cu nanowires prepared at relatively low temperatures, e.g., 150 and 200 ^{o}C, have a typical diameter of 100 nm and lengths varying from 20 to 50 μm. Slightly thicker and shorter nanowires were obtained by hydrogen reduction at higher temperatures, with the extent of deformation dependent on the time of annealing. For 1 hour at 300 ^{o}C, long (>20 μm) nanowires were still observed, whereas the majority were found to be shorter than 20 μm after annealing for 15 hours at this temperature.

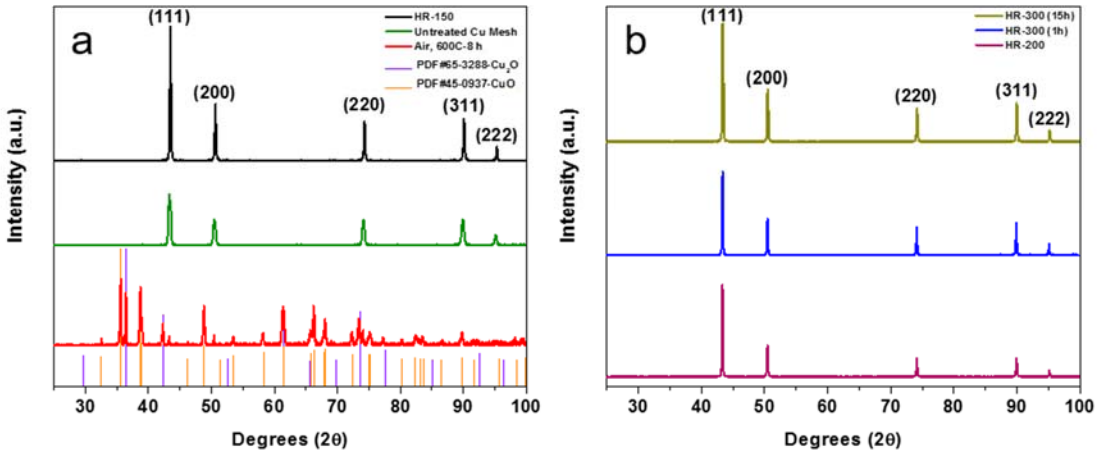

Figure S2. (a) XRD patterns of the pristine Cu mesh, after annealing in air (600 ^{o}C), and the HR-150 Cu nanowires. Metallic Cu facets are denoted with respective peak assignments. Peaks for CuO and Cu_2O are marked at the bottom for comparison. (b) XRD patterns of HR-200, HR-300 (1h) and HR-300 (15h). After annealing in air at 600 °C, Cu is oxidized into CuO and Cu_2O, with latter likely being an intermediate layer between the formed CuO nanowires and residue metallic Cu in the mesh.[6] After reduction by hydrogen, the crystal phase transforms back to metallic Cu, indicating the reduction of the CuO nanowires into Cu nanowires.

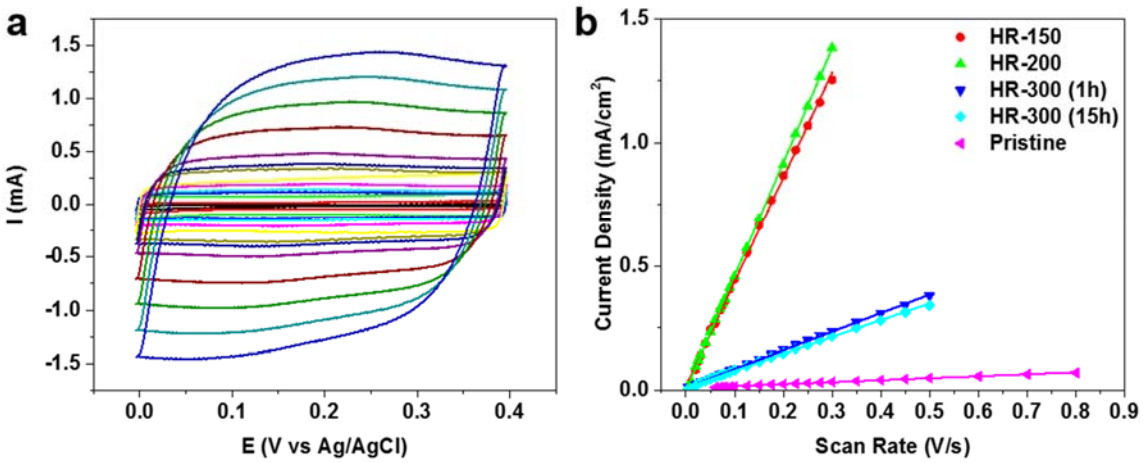

Figure S3. (a) CVs recorded for the HR-150 Cu nanowires used for capacitance measurements. (b) Plot of the width of double-layer region in the CV versus the scanning rate with the slope used to determine the capacitance (see Table S1 below).

Table S1. Summary of the roughness factors of the Cu electrodes studied in this work.

Sample	Capacitance (mF/cm²)	Surface Roughness Factor
Untreated Cu Mesh	0.081	2.8
HR-300 (15h)	0.676	23
HR-300 (1h)	0.748	26
HR-200	4.60	158
HR-150	4.22	145

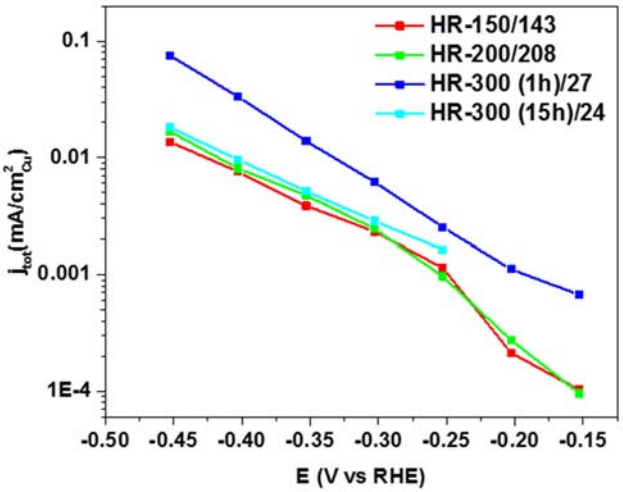

Figure S4. Current densities of CO reduction per ECSA of Cu.

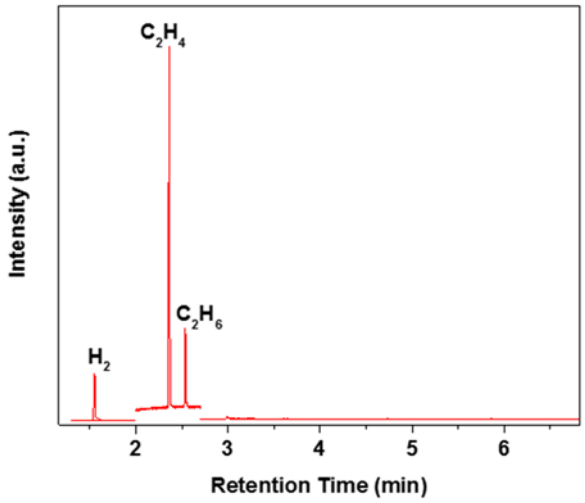

Figure S5. Representative GC-MS spectrum recorded for the gas-phase products derived from the HR-150 Cu nanowires @ −0.45 V.

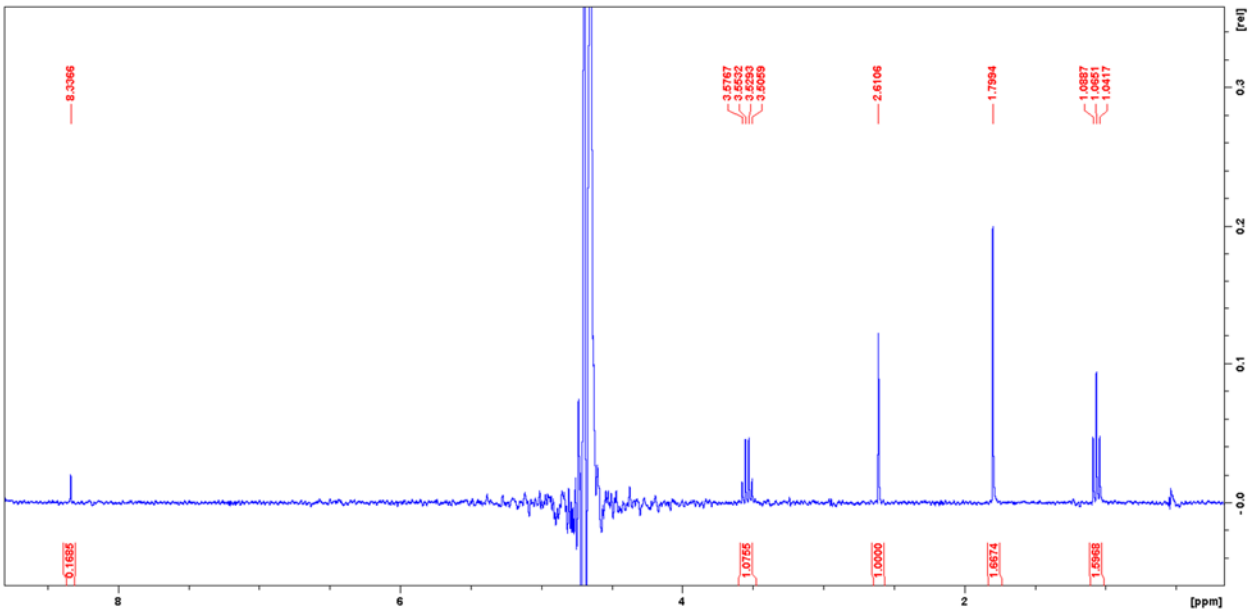

Figure S6. Representative NMR spectrum collected for the liquid products from CO reduction by using the HR-150 Cu nanowires at −0.3 V. The spectrum was acquired on a Bruker 400 MHz NMR spectrometer using a 5 mm bbo probe with 2 scan delay, 10.09 degree read-pulse, and over 8278 Hz spectral width, for 16 scans. The peak in the center of the spectra is the suppressed water peak. Assignment of all the observed peaks is given in Table S2.

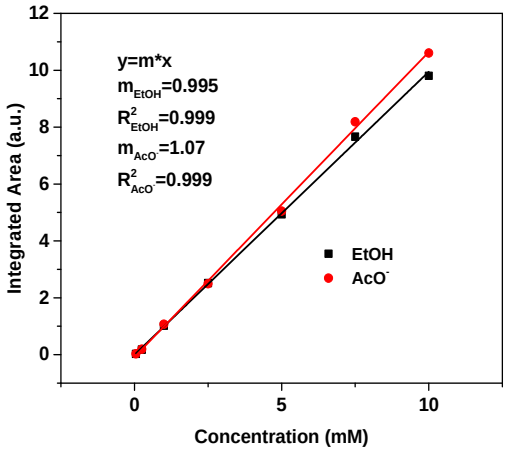

Figure S7. Calibration curves generated for the major liquid products, acetate and ethanol, in NMR analysis.

Table S2. Peak assignment and data from the NMR analysis corresponding to the spectrum shown in Figure S6. The observed peaks were compared to commercially available standards. The row highlighted in orange indicates the internal standard used to quantify the concentrations of CO reduction products. For ethanol, the triplet peak (highlighted in blue) was used for quantitation because of its higher intensity when compared to the other peaks.

Experimental Observation			Assignment		Known Standards		
Chemical Shift (ppm)	^{1}H splitting	J coupling	Probed Nucleus	Product Name	Chemical Shift (ppm)	^{1}H splitting	J coupling
0.78	t	7.37	$CH_3CH_2CH_2OH$	n-Propanol	0.77	t	7.57
1.07	t	7.06	CH_3CH_2OH	Ethanol	1.06	t	7.08
1.42	sextet	6.742	$CH_3CH_2CH_2OH$	n-Propanol	1.42	sextet	7.32
1.8	s	-	$CH_3C(=O)O$	Acetate	1.87	s	-
2.61	s	-	DMSO	Internal Standard	2.6	s	-
3.45	t	6.7	$CH_3CH_2CH_2OH$	n-Propanol	3.44	t	6.49
3.53	q	7.07	CH_3CH_2OH	Ethanol	3.53	q	7.32
			Water				
8.34	s	-	$HCOO^-$	Formate	8.33	s	-

Table S3. Summary of total geometric current densities for CO reduction (j_{TCP}) and the Faradaic efficiencies of different products at various potentials on the HR-150 Cu nanowires.

E	j_{TCP}	Faradaic Efficiency (%)				
V vs RHE	mA/cm$^2_{geo}$	C_2H_4	C_2H_6	AcO^-	EtOH	1-PrOH
-0.153	0.00	0.58	0.51	6.90	0.00	0.00
-0.203	0.00	0.23	0.17	13.15	0.00	0.00
-0.253	0.08	0.09	0.09	21.56	28.31	0.00
-0.303	0.22	0.66	0.48	14.50	49.79	0.00
-0.353	0.32	2.69	1.55	9.84	43.37	0.00
-0.403	0.38	5.79	2.55	2.58	21.96	1.03
-0.453	0.43	6.49	1.80	0.74	10.61	1.50

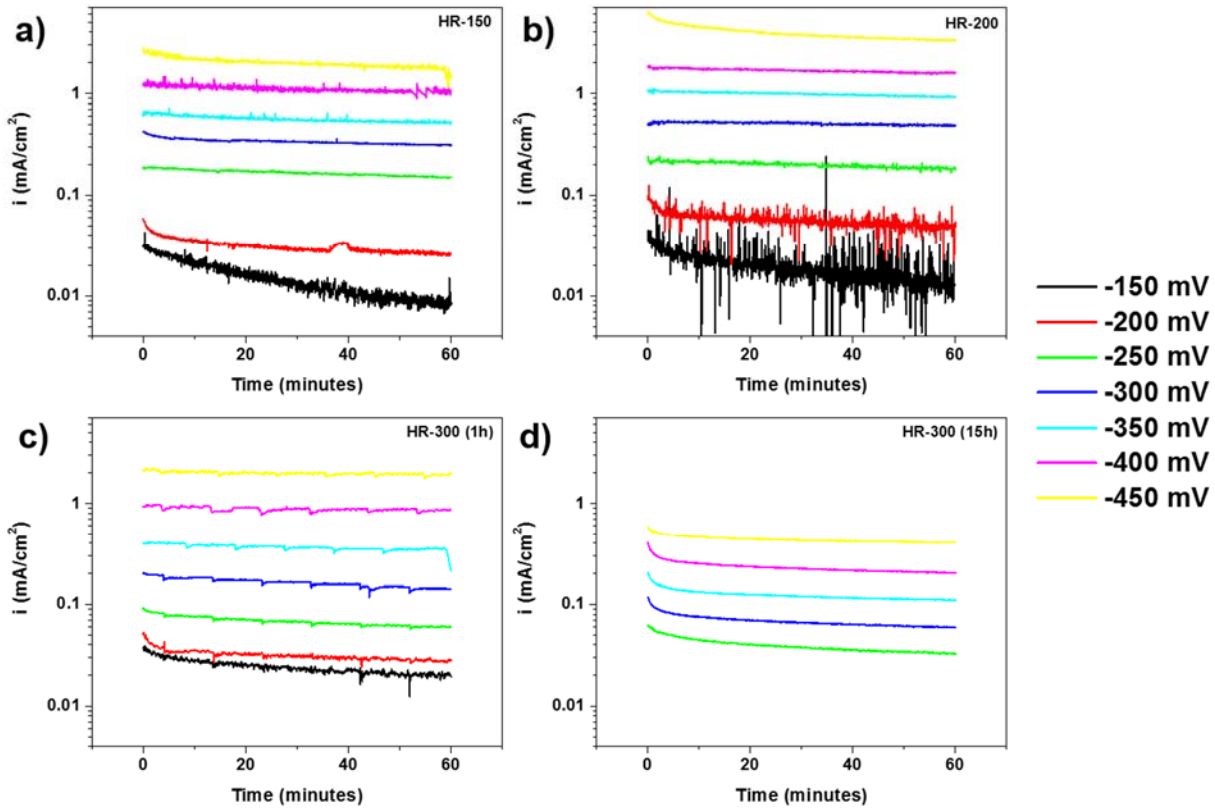

Figure S8. Dependence of total current density (j_{tot}) on time at all potentials investigated for the Cu nanowire catalysts.

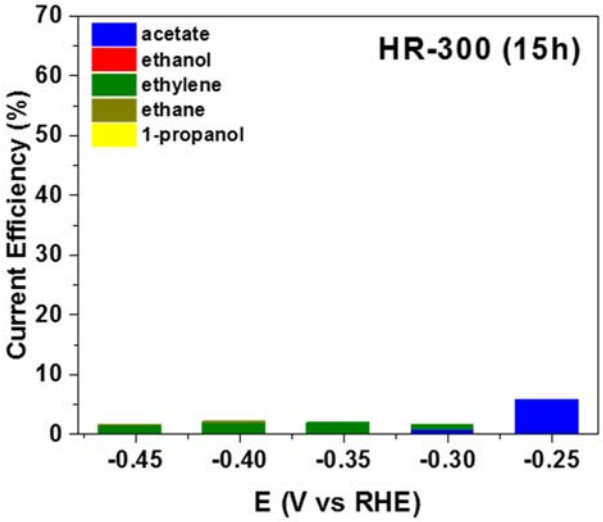

Figure S9. Faradaic efficiencies of hydrocarbons produced via CO reduction using HR-300 (15h) Cu nanowires.

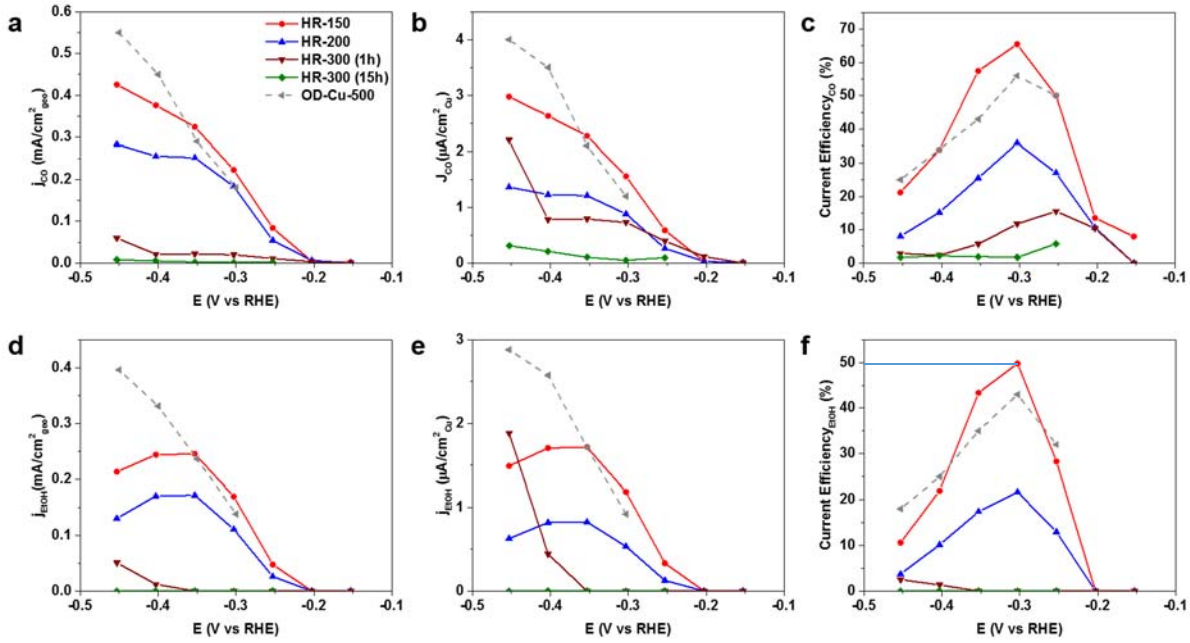

Figure S10. Comparison of the nanowire catalysts reported in this work with the OD-Cu-500 electrode reported by Kanan *et al.*[7] It can be seen that the HR-150 nanowires outperformed the cuprite-derived Cu electrodes at potentials more positive than −0.35 V, in particular with a positive shift of the onset potential by ~100 mV; The peak FEs have also been raised from ~55% to 65% for CO reduction and from ~42% to 50% for ethanol at ca. −0.30 V.

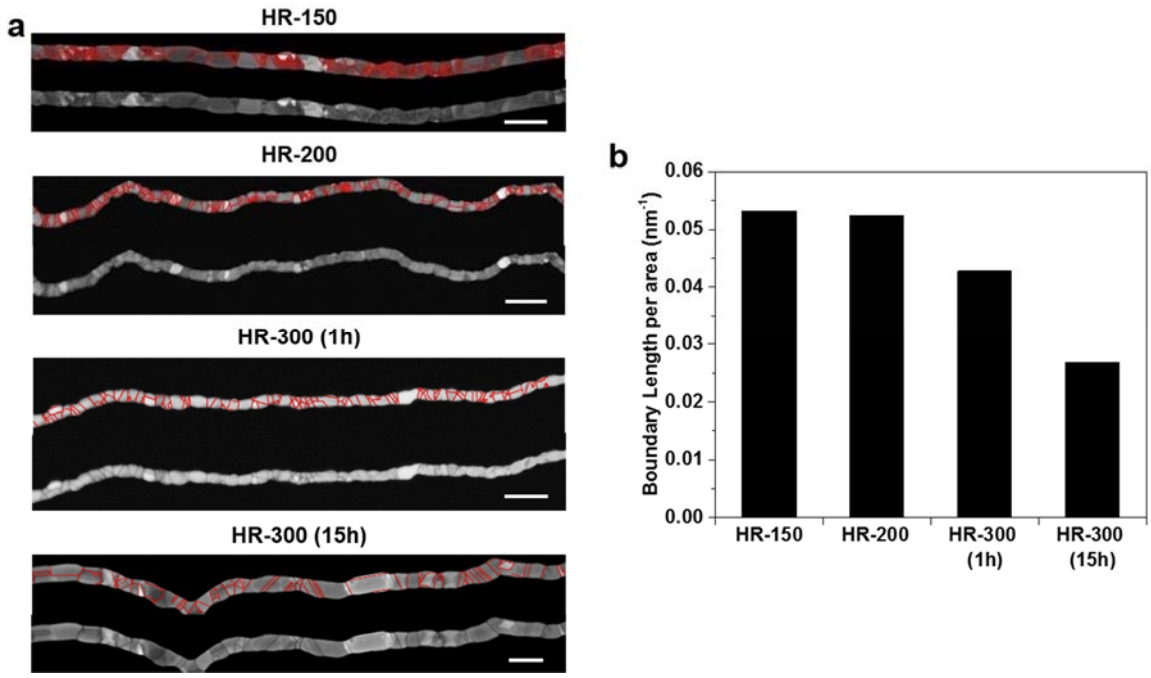

Figure S11. Crystalline structures of the Cu nanowires. (a) Crystalline domain structures derived from SPED analysis for the Cu nanowires. For each type of nanowire in (a), the left is the TEM image and the right shows the crystal boundaries marked in red (scale bar = 200 nm). (b) Dependence of crystal boundary density on the preparation temperature for the Cu nanowires.

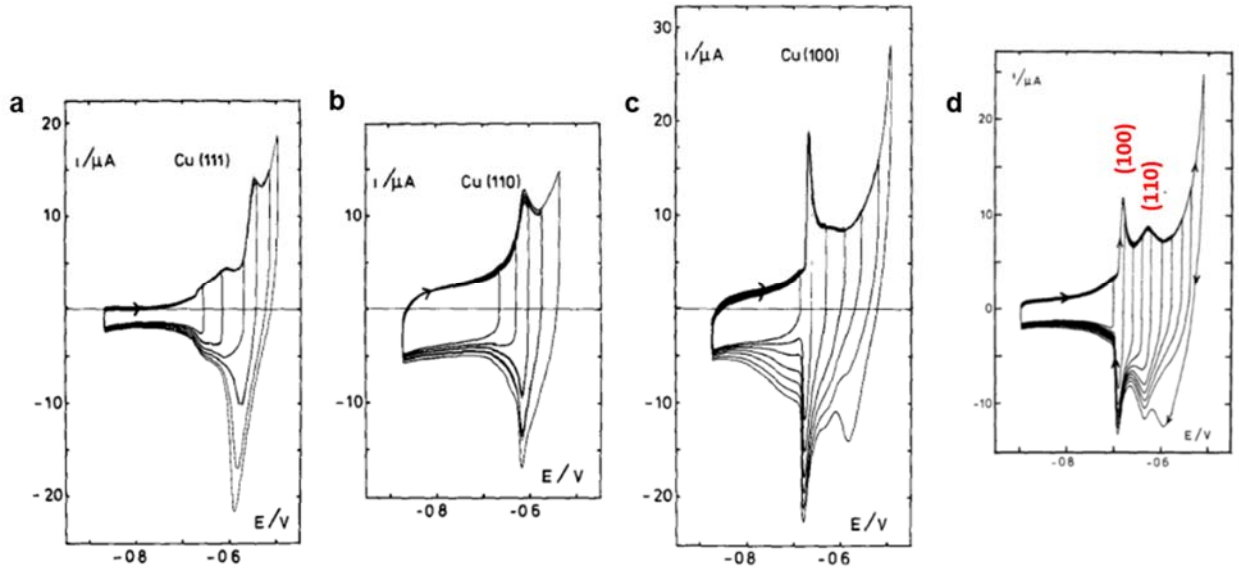

Figure S12. CVs of single-crystal (a-c) and polycrystalline (d) Cu electrodes as reported by Droog and Schlenter.[3] Recorded at 20 mV/s in 1 M NaOH. The potentials were given against Ag/AgCl.

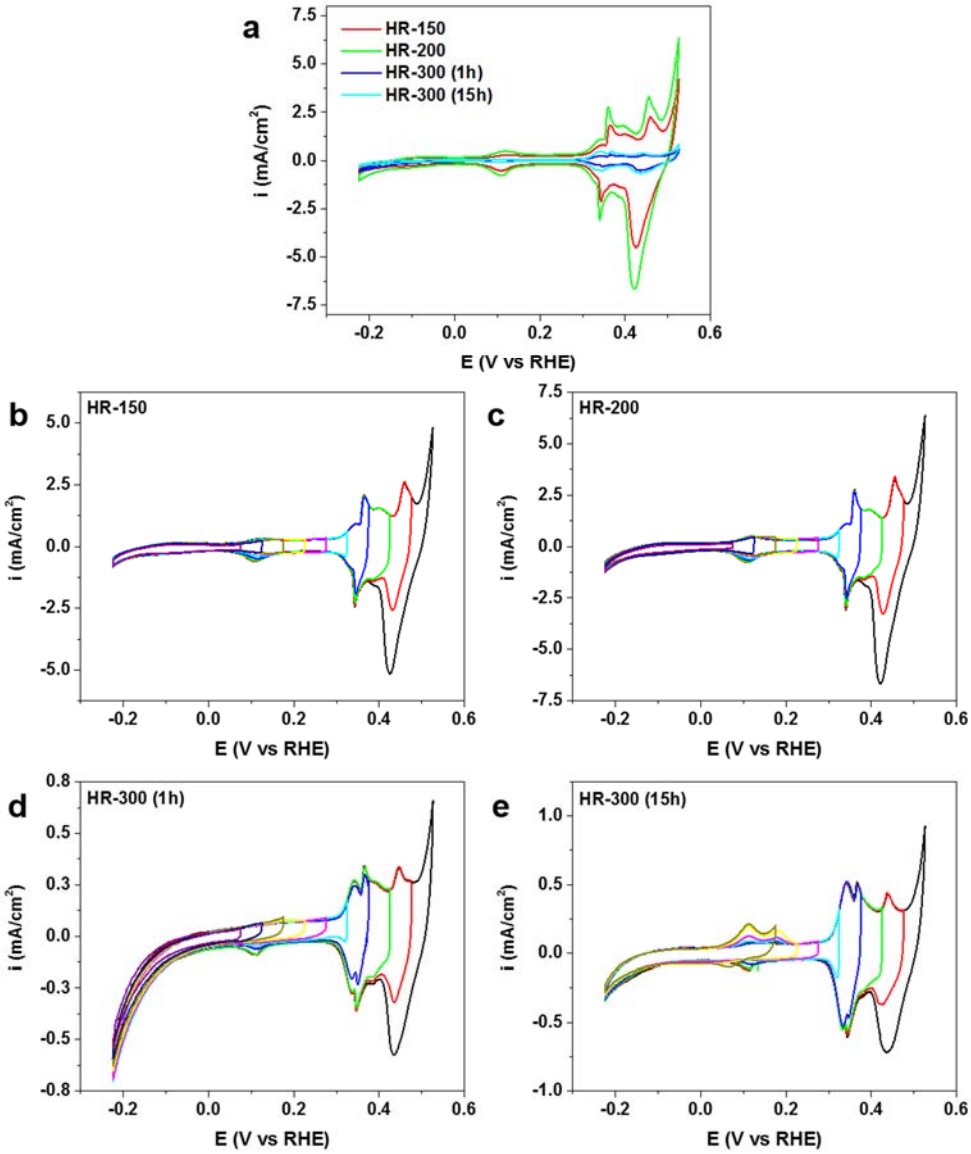

Figure S13. Cyclic voltammograms (CVs) recorded at 20 mV/s in 1 M KOH for the different types of Cu nanowires. The OH_{ad} peaks are assigned to the Cu facets according to the results reported on single crystals (as shown in Figure S12). The upper potential limit was carefully selected to ensure that all the features were reproducible in successive scans.

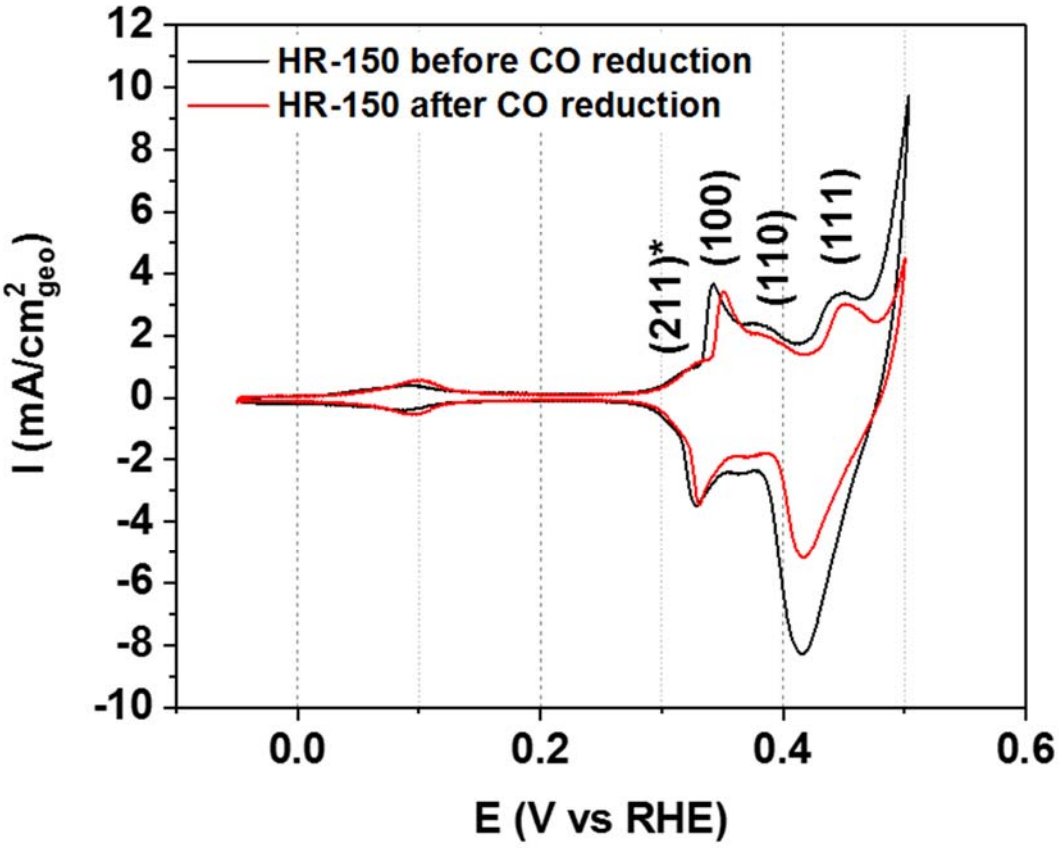

Figure S14. CVs before and after CO reduction showing the stability of the surface structure features.

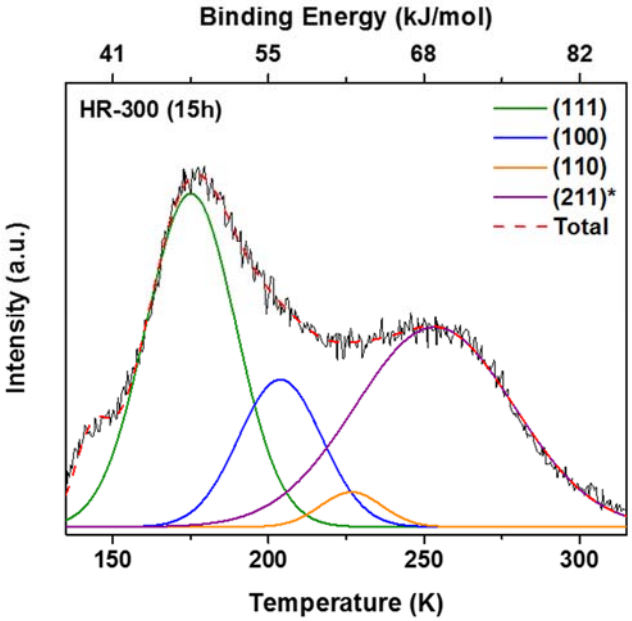

Figure S15. CO-TPD pattern recorded on the HR-300 (15h) Cu nanowires.

S3. DFT Calculations

Computational Methods. Density functional theory (DFT)[8] calculations were performed to find the lowest free-energy pathways for CO reduction to C_2 products. All DFT calculations were performed with the Vienna Ab initio Simulation Package (VASP)[9, 10], in which the Kohn-Sham equations are solved by self-consistent algorithms. The C_GW_new, Cu_pv_GW, H_GW, and O_GW PBE projector-augmented wave (PAW)[11] potentials provided with VASP were used to improve the calculation efficiency, and VASP was run with high precision. The revised Perdew-Burke-Ernzerhof (RPBE)[12, 13] exchange-correlation functional was used for all DFT-calculations unless otherwise noted. Van der Waals interactions were accounted for by using the DFT-D3 method[14] (which we will refer to as RPBE-D3), which has been shown to result in accurate calculated properties for water and small organic molecules on metal surfaces.[15-18] The calculations without inclusion of van der Waals interactions are referred to as RPBE calculations. Spin polarization was taken into account in the calculations and the Methfessel–Paxton method[19] of order 2 was employed to determine electron occupancies with a smearing parameter of 0.2 eV. The convergence criteria for the electronic self-consistent iteration and the ionic relaxation loop were set to be 10^{-4} eV and 10^{-3} eV, respectively. To treat the effects of the aqueous solvent on adsorption energies, we have used the VASPsol implicit solvation method.[20, 21]

The Brillouin zone was sampled using grids generated by the *k*-point grid server[22] with a minimum distance of 46.5 Å between real-space lattice points. The shift vectors were automatically chosen to minimize the number of irreducible *k*-points, and the grids were automatically optimized for slab calculations. For all four surface slabs representing different Cu facets, the lattice constant was fixed to the calculated lattice constant for a relaxed bulk Cu fcc crystal (3.65 Å). On the fcc(111) surface, calculations were performed on a 3×3 periodic unit cell with a 4-layer slab and 15 Å of vacuum. The fcc(100) facet used a 3×3 periodic unit cell with a 4-layer slab and 16 Å of vacuum. Also, the fcc(110) facet used a 3×3 periodic unit cell with a 3-layer slab and 16 Å of vacuum. The fcc(110) reconstructed facet, denoted as (110)-rec, was created

by introducing a (1×2) missing row, which has a 4×2 periodic unit cell with a 3-layer slab and 16 Å of vacuum. Moreover, the fcc(211) facet used a 4×3 periodic unit cell with a 4-layer slab and 16 Å of vacuum. The unit cells for clean slabs of these Cu facets: Cu(111), Cu(100),Cu(110), Cu(110)-rec, and Cu(211) are as shown in Figure S16. For the calculations of binding energies of adsorbates, during structure optimization, the 2 bottom layers were fixed at the optimized bulk positions to mimic the bulk crystal structure beneath the surface, while the adsorbates and the topmost layers were allowed to relax in all directions. For the calculations of free energies of different facets, all atoms are allowed to fully relax. We have tested for the convergence with respect to slab thickness in terms of surface energies of clean slabs and *CO adsorption energies on all five fcc(111), fcc(100), fcc(110), fcc(110)-rec and fcc(211) facets. The convergence criteria for surface energy and *CO adsorption energy were 1~2 meV/Å^2 and 10 meV, respectively.

Computational Hydrogen Electrode (CHE) Model. In the computational hydrogen electrode (CHE)[23] model, at 0 V (vs RHE), the chemical potential of a proton-electron pair, $\mu(\mathrm{H^+}) + \mu(\mathrm{e^-})$ is equal to half of the chemical potential of gas-phase hydrogen molecule $\frac{1}{2}\mu(\mathrm{H_2(g)})$ at 101,325 Pa, at all pH values, and at all temperatures. Thus, the chemical potential of the proton-electron pair can be adjusted as a function of applied potential by the standard relation between chemical and electrical potential, $\Delta\mu = -eU$. Thus, the total value of $\mu(\mathrm{H^+}) + \mu(\mathrm{e^-})$ as a function of applied potential at all temperatures and pH values can be expressed as follows:

$$\mu(\mathrm{H^+}) + \mu(\mathrm{e^-}) = \frac{1}{2}\mu(\mathrm{H_2(g)}) - \mathrm{eU} \qquad (2)$$

The free energy change for each intermediate step that involves an electron transfer will be a function of the applied electrical potential (*U*). As the electrical potential is lowered to more negative in the CHE model, the free energies of the adsorbates with n pairs of electron-proton transfer referenced to CO(g) will decrease by ne*U*. The entire reduction pathway will become

exergonic (downhill in the free energy diagram from left to right) when the applied potential is sufficiently low. The potential at which the pathway first becomes exergonic is the calculated upper (i.e. least negative) bound for the onset potential of the pathway.

Surface Energies. The surface energies of the different Cu and CuO facets were performed using spin-polarized DFT calculations with the PBEsol[24] exchange correlation functional. The PBEsol exchange-correlation functional has been shown to give more accurate results than RPBE for surface energies for metals[25, 26] including Cu.[27] To correct for the tendency of DFT to over-delocalize the electrons in transition-metal oxides such as CuO, we have used the DFT+U method as developed by Dudarev et al.[28] with a $U_{\text{eff}} = U - J$ value of 6.52 eV[29] for CuO surfaces. All CuO slabs and Cu slabs are (1x1) primitive cells with thicknesses of greater than 15 Angstroms. The vacuum layers in between are also greater than 15 Angstroms thick. Taking Cu surface as an example, the surface energy is defined as:

$$E_{surf} = \frac{E_{slab}^{DFT} - \frac{N_{slab}}{N_{bulk}} * E_{bulk}^{DFT}}{2 * A}, \qquad (3)$$

where E_{slab}^{DFT} is the DFT energy of per unit cell of a Cu slab with all atoms allowed to relax in all directions and lattice parameter in the direction parallel to the surface fixed to be the same as bulk lattice parameter, E_{bulk}^{DFT} is the energy of per unit cell of the Cu bulk crystal, N_{slab} is the number of atoms per unit cell of the slab, N_{bulk} is the number of atoms per unit cell of the bulk crystal, and A is the surface area of one side of the slab. For each slab we have two surfaces, which is reflected by the number 2 in the denominator in equation (3). The slabs were constructed to ensure that the upper and lower surfaces of the slab were symmetrically equivalent. The calculated surface energies for different Cu and CuO facets are listed in Table S4 and

Table S5.

Free Energies of Adsorbates. We calculated the free energy change of the CO reduction intermediates at zero potential (*U*=0) as,

$$\Delta G(U=0) = \Delta E_{DFT} + \Delta ZPE - T\Delta S + \Delta \int_{T'=0}^{T} C_P \mathrm{d}T', \quad (4)$$

where ΔE_{DFT} is the electronic energy for the intermediate step of the CO reduction directly obtained from DFT calculations, ΔZPE is the difference in zero point energies corresponding to the certain reaction, ΔC_P is the difference in constant-pressure heat capacities, ΔS is the change in entropy, and T is the temperature (we choose 291.65K, to be consistent with the work of Peterson et al.[30]). Values for the last three terms in equation (4) are listed in Table S6 and Table S7 below. Our free energy diagrams were constructed assuming a CO partial pressure of 1 atm (1.01325E5 Pa), to be consistent with the measured pressure obtained from the mass flow controller (Alicat). At an applied potential *U*, the total change in free energy is calculated by

$$\Delta G(U) = \Delta E_{DFT} + \Delta ZPE - T\Delta S + \Delta \int_{T'=0}^{T} C_P \mathrm{d}T' - eU \quad (5)$$

Here, e is the number of $(H^+ + e^-)$ that have been transferred.

The electronic energies of all intermediate states reported in the present paper are calculated using the lowest-energy bonding sites and optimized geometries for *CO, 2*CO, *CHO, *COH, *CO+*CHO, 2*CHO, *OCHCHO*, *COCHO, and *COCOH. ΔE_{DFT} for adsorbates are calculated as the electronic energy of the state minus the electronic energy of corresponding clean slab (Cu(211), Cu(110), Cu(110)-rec, Cu(100) and Cu(111)), with C atoms referenced to graphene, H atoms to 1/2 H_2, and O atoms to (H_2O-H_2). Here is an example for *CO,

$$\Delta E_{DFT}(*\mathrm{CO}) = E_{DFT}(*\mathrm{CO}) - \mathrm{E}_{DFT}(*) - \mathrm{E}(\mathrm{C(graphene)}) - \mathrm{E}(\mathrm{H_2O}) + E(\mathrm{H_2}), \quad (6)$$

where $E(\mathrm{O}) = E(\mathrm{H_2O}) - E(\mathrm{H_2})$.

In the work of Blaylock et al.[31], the gas-phase thermodynamic reaction energies calculated

using RPBE functional were particularly inconsistent with experimental reference values. In this paper, the CO reduction involves gas-phase molecules of CO, H_2, and H_2O, and the initial state of free energy diagrams is the free energy of CO(g). Thus we evaluated whether it was necessary to apply a gas-phase free-energy correction to our DFT calculations by comparing calculated and experimental gas-phase reaction enthalpies at 25 °C and 101325 Pa, using the same method as Peterson et al.[30] The reactions we chose are listed in Table S8. As shown in Table S9, the average and standard deviation of reaction enthalpy errors for RPBE gas-phase values in reactions containing CO(g) were -0.04 eV and 0.02 eV, respectively, which are relatively small. Thus, we decided not to apply any gas-phase free energy corrections for the DFT calculations in this paper.

It has been shown that for small organic molecules on metal surfaces, using an exchange-correlation functional that accounts for van der Waals interactions can result in more accurate calculated adsorption energies.[15, 32-34] To evaluate the ability of different exchange-correlation functionals to accurately model adsorption energies we have calculated OH and CO binding energies using both RPBE and RPBE-D3. We have also evaluated the optB86b-vdW functional[35-37] (which we will refer to as optB86b) as a potential alternative to RPBE-D3. The experimental order of *OH binding strength is Cu(211) > Cu(100) > Cu(110) > Cu(111) (Figure 3a), and the experimental order of *CO binding strength is Cu(211) > Cu(110) > Cu(100) > Cu(111) (Figure 3b).[3, 5] According to Table S10 and Table S11, among the RPBE, RPBE-D3, and optB86b methods, RPBE-D3 is the only functional we tested that gets the order of adsorbate binding energies on Cu surfaces in agreement with experiments for both CO and OH. RPBE is in agreement with experiments for CO but not OH; optB86b method is in agreement with experiments for OH but not CO.

We note that RPBE-D3 likely overestimates the free energy change from *CO to *CHO, as it is known to anomalously overbind CO.[15, 38] On the other hand, RPBE without the van der Waals correction calculates CO adsorption energies that are close to experimental values.[26, 39] Using RPBE, we calculate CO adsorption energies of 70, 63, 58, and 51 kJ / mol on the (211),

(110), (100), and (111) facets respectively (Table S11 and Figure 4b), which are in excellent agreement with the experimental energies of 71, 63, 56, and 49 kJ / mol on the (211), (110), (100) and (111) derived from the CO TPD data on HR-150 nanowires (Figure 3b). The data in Table S12 suggests that the RPBE-D3 free energies for *CO are about 0.3 eV too low. Thus, for the free energy diagrams constructed in this paper, we have used plain RPBE to calculate the adsorption energies of *CO and 2*CO, used an average of the RPBE and RPBE-D3 values to calculate the adsorption energy of *CO+*CHO, and used the RPBE-D3 adsorption energies for other adsorbates.

Free Energy Diagrams. The catalytic activities and selectivities of the Cu nanowires for CO reduction (Figures 1 and Figure 2) are correlated with the fractions of Cu(110) facets on the surface (Figure 3). To understand this correlation and the mechanism of CO reduction to C_2 species, we have performed DFT calculations for possible pathways on the five types of Cu facets: Cu(211), Cu(110), Cu(110)-rec, Cu(100) and Cu(111), because experimental data (Figure 3) indicates that these facets are the most prevalent facets on the synthesized Cu nanowire.

We consider three possible paths for the reduction of CO to C_2 species on each of these surfaces. The first two paths start with the protonation of adsorbed CO (denoted *CO) to form either *COH or *CHO.[40-42] The third mechanism involves the direct coupling of CO molecules to form an $OCCO^{\delta-}$ dimer as an intermediate species,[43] which we will refer to as CO-CO coupling mechanism. This mechanism has been proposed to explain the observation that on the Cu(100) surface C_2 products are formed at low overpotentials (versus RHE) without the formation of C_1 products.[44, 45] The $OCCO^{\delta-}$ dimer is believed to become negatively charged prior to a proton transfer, which would explain the observed pH-dependence of the overpotential on the Cu(100) facet versus the RHE.

To model these three mechanisms we have used the computational hydrogen electrode (CHE)[23] approach, in which the free energy of $(H^+ + e^-)$ is calculated using the fact that $(H^+ + e^-)$ is in equilibrium with $(1/2)H_2(g)$ at zero potential versus the RHE. The calculated onset potential

is the least negative applied potential at which all reaction steps become exergonic. The onset potentials we calculate are estimates of the upper bounds of the true onset potentials, as we do not include intermediate states for which the uncertainty in the free energy is high. Specifically, we do not calculate the free energies of the unstable transition states between intermediates, as these depend on the exact path of the transition and the molecular structure of the solvent, which we have not investigated here. However, such kinetic effects may be important, for example, in differentiating the *CHO and *COH pathways in aqueous solution if the free energies of *CHO and *COH are similar.[41, 46] In addition, we do not calculate the free energy of the charged*$OCCO^{\delta-}$ intermediate in the CO-CO coupling mechanism, which depends on both the pH and the applied potential. Accurately calculating the free energy of this intermediate using DFT is challenging; different approaches for calculating the free energy for the transition from 2*CO to *$OCCO^{\delta-}$, involving different treatments of solvent and the applied potential, produce values that differ by more than 1 eV.[47, 48]

Figure S17 shows the predicted free energies on the path from CO(g) to *CHO on Cu(211), Cu(110), Cu(110)-rec, Cu(100), and Cu(111) facets. The corresponding free energy barriers for the formation of *CHO are 0.48 eV, 0.27 eV, 0.40 V, 0.40 eV, and 0.57 eV respectively, which are lower than the values predicted by previous computational works.[30, 46, 49] For example, on the Cu(211) facet, the calculated rate-limiting step for CO_2 reduced to CH_4 was reported to be from *CO to *CHO, with a calculated free energy difference of 0.74 eV at zero applied potential.[30] In the work of Durand et al.[49], the free energy barriers from *CO to *CHO are about 0.7 eV, 0.8 eV, and 0.9 eV for Cu(211), Cu(100) and Cu(111) facets respectively. Our calculated free energy barriers are lower than these values by an amount of about 300 meV primarily due to the inclusion of van der Waals interactions for adsorbates other than *CO.

We find that the formation of *CHO is more thermodynamically favorable than the formation of *COH on the (110), (110)-rec, (111) and (211) surfaces, and the free energies of *CHO and *COH are similar on the (100) surface, consistent with previous studies.[41, 50] Calculated

free energy values are provided in Table S12. On the (110) facet, the free energy of *CHO is 891 meV less than the free energy of *COH. The magnitude of this difference suggests that the *CHO path would be preferred on this surface even if kinetics were fully considered.

After the formation of *CHO, it has been proposed that C_2 species form via an *OCHCHO* intermediate,

$$2CO(g) \rightarrow CO(g) + *CO \rightarrow 2*CO \rightarrow *CO + *CHO \rightarrow 2*CHO \rightarrow *OCHCHO*, \quad (7)$$

and after the formation of *OCHCHO* additional protonation to form C_2 products should proceed rapidly.[40] The pathway in equation (7) is referred as CHO-CHO coupling mechanism. On all four surfaces, we predict the coupling of carbon atoms to form *OCHCHO* to be relatively facile (Figure 4c), so that the rate-limiting step for the *OCHCHO* path is the protonation of *CO to form *CHO. The calculated minimum onset potentials for the CHO-CHO coupling mechanism are -0.48, -0.36, -0.43, -0.45, and -0.57 V on the (211), (110), (110)-rec, (100), and (111) surfaces respectively (Figure 4c), indicating that the (110) surface would be most active for this mechanism. These calculated onset potentials are somewhat smaller (in absolute value) than other studies.[30, 41, 49] This is likely because we do not calculate the free energies of transition states, and because we include van der Waals interactions in our calculations for adsorbates other than CO, which reduces the magnitude of the calculated onset potential by significantly decreasing the free energies for hydrogenated adsorbates (Table S12). We have mentioned in the main text that strongly adsorbed *OH may limit CO reduction at low overpotentials. Similarly, the *CO coverage may also affect our calculated onset potentials: The free energy diagrams and the calculated onset potentials in Figure 4 are based on the DFT calculations of surfaces with low *CO coverage (1/12 ML on the (211), and 1/9 ML on the (110), (110)-rec, (100), and (111) for single *CO adsorbate), and DFT calculations of higher *CO coverages will likely give us different values of onset potentials.

We find a similar trend for the CO-CO coupling pathway:

$$2CO(g) \rightarrow CO(g) + *CO \rightarrow 2*CO \rightarrow *COCHO \text{ or } *COCOH . \quad (8)$$

The calculated upper bounds of the onset potentials, again using the RPBE value for the free energy of *CO, are -0.68, -0.34, -0.49, -0.31, and -0.53 V on the (211), (110), (110)-rec, (100), and (111) surfaces respectively (Figure 4d). The rate-limiting step is

$$2*CO + H^+ + e^- \rightarrow COCHO \text{ or } *COCOH . \quad (9)$$

Alternatively, CO-CO coupling could occur through an Eley-Rideal mechanism:

$$*CO + CO(g) + H^+ + e^- \rightarrow *COCHO \text{ or } *COCOH . \quad (10)$$

In this case, the calculated upper bounds on the onset potentials are -0.53, -0.14, 0.37, -0.20, and -0.53 V on the (211), (110), (110)-rec, (100), and (111) surfaces respectively. In both of the above steps, we have skipped over the likely formation of the $*OCCO^{\delta-}$ intermediate, due to the aforementioned uncertainty in the calculated free energy for this state. Under conditions in which the $*OCCO^{\delta-}$ state has greater free energy than *COCHO or *COCOH, the onset potentials would be more negative than the upper bounds listed above. However, at sufficiently high pH, the free energy of the $*OCCO^{\delta-}$ state will drop below the free energies of *COCHO and *COCOH, making the formation of *COCHO and *COCOH the rate-limiting step for C-C coupling. The CO-CO coupling mechanism could potentially then proceed on the (110) surface at very low overpotentials versus the RHE.

Although the Cu(110) surface could be capable of reducing CO to C_2 products at very low overpotentials, the observation of Cu(110) on the reduced nanowires is of interest (Figure 3), as it has the highest calculated surface energy (Figure 4a in the main text, and also see Table S4), and it does not show up on a calculated Wulff construction of the equilibrium crystal shape for Cu.[51] To understand why the reduction of CuO results in the creation of high-energy Cu(110) surfaces, we have calculated the surface energies for the "equivalent" CuO surfaces (Table S5), which are those that would relax to a Cu(110) surface if all oxygen disappeared from a CuO crystal (Figure S18). We similarly consider CuO surfaces that are equivalent to Cu(100), Cu(111), and

Cu(211). The CuO surfaces with the lowest surface energy are equivalent to the Cu(111) surface, followed closely by the CuO(011) surface, which is equivalent to the Cu(110) surface. Thus it is possible that some low-energy CuO(011) surfaces transform into high-energy Cu(110) surfaces upon reduction. Because the Cu(110) surfaces are not thermodynamically stable, they will disappear after annealing at sufficiently high temperature for sufficiently long time, explaining why ECR and HR-150 nanowires have a much higher percentage of Cu(110) facets than HR-300 nanowires (Figure 3c).

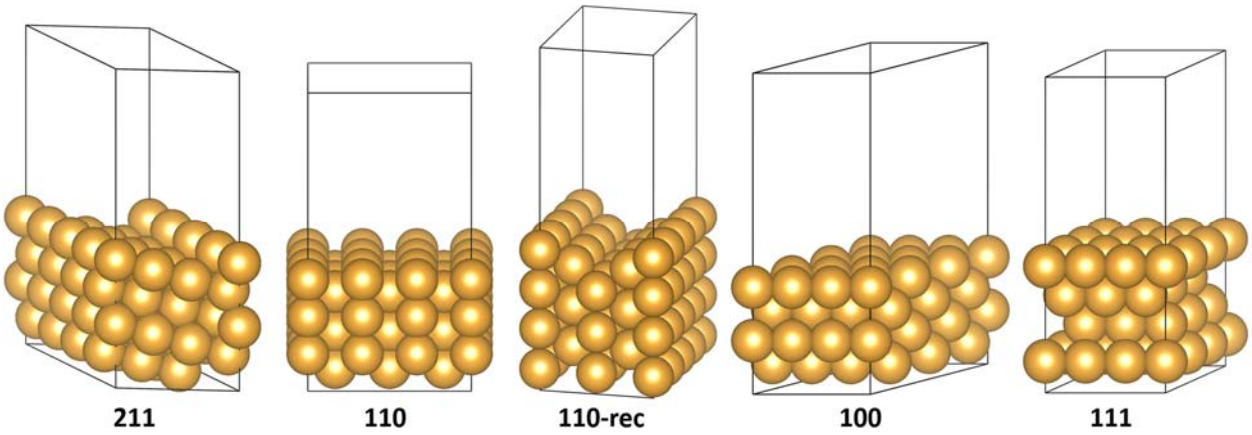

Figure S16. Unit cells for clean slabs of these five Cu facets: Cu(211), Cu(110), Cu(110)-rec, Cu(100) and Cu(111). Golden spheres represent the Cu atoms.

Table S4. Calculated surface energies for various Cu facets.

	Facet	Surface energy (meV/Å^2)	Surface energy (J/m^2)
Cu	(1 0 0)	94.85	1.518
Cu	(1 1 0)	100.35	1.606
Cu	(110)-rec	100.22	1.603
Cu	(1 1 1)	84.58	1.353

Cu	(2 1 1)	96.84	1.549

Table S5. Calculated surface energies for various CuO facets. Here, * stands for oxygen-terminated surfaces.

	CuO facet	Equivalent facet	Surface energy (meV/Å^2)	Surface energy (J/m^2)	Reference values (Mishra et al.[52]) (J/m^2)
CuO	*(0 1 0)	Cu (100)	90.21	1.44	1.35
CuO	(0 0 1)		106.71	1.71	-
CuO	*(1 0 0)		110.87	1.77	1.68
CuO	(1 0 0)		112.53	1.80	1.83
CuO	*(0 1 1)	Cu (110)	64.58	1.03	0.94
CuO	(0 1 -1)		64.25	1.03	-
CuO	(1 0 1)		71.64	1.15	1.17
CuO	(1 0 -1)		76.81	1.23	-
CuO	(1 1 0)		85.70	1.37	1.37
CuO	(-1 1 0)		91.96	1.47	-
CuO	(1 1 1)	Cu (111)	50.84	0.81	0.75
CuO	(1 -1 -1)		62.63	1.00	0.89
CuO	(1 1 -1)		66.94	1.07	-
CuO	(1 -1 1)		82.17	1.31	-
CuO	(1 1 2)	Cu (211)	91.25	1.46	-
CuO	(1 2 1)		93.71	1.50	-
CuO	(2 1 1)		100.51	1.61	-

Table S6. Zero point energies corrections ($ZPEs$), enthalpic temperature corrections ($\int C_P \mathrm{d}T$), and entropy contributions (TS) for adsorbed species in the present paper. Here, the data for *H, *CO, *CHO, and *COH are from the work of Peterson et al.[30] The data for *COCHO, *COCOH, and *OCHCHO* are from the work of Calle-Vallejo et al.[43]

adsorbate	ZPE (eV)	TS (eV)	$\int C_P \mathrm{d}T$ (eV)
*H	0.16	0.007	0.005
*CO	0.192	0.153	0.076
*CHO	0.444	0.184	0.086
*COH	0.451	0.11	0.068
OCHCHO	1.03	0.22	0.12
*COCHO	0.68	0.25	0.12
*COCOH	0.70	0.24	0.12

Table S7. Zero point energies corrections ($ZPEs$), enthalpic temperature corrections ($\int C_P \mathrm{d}T$), and entropy contributions (TS) for non-adsorbed species used in the present paper are from the work of Peterson et al,[30] and the data for C_2H_2 and C_2H_6 are from the work of Calle-Vallejo et al.[43]

species	ZPE (eV)	TS (eV)	$\int C_P \mathrm{d}T$ (eV)
CO_2	0.31	0.65	0.10
CO	0.14	0.67	0.09
CO(1 atm)	0.14	0.60	0.09
H_2	0.27	0.42	0.09
H_2O	0.58	0.65	0.10
CH_4	1.20	0.60	0.10
C_2H_2	0.72	0.62	0.10
C_2H_4	1.36	0.71	0.11
C_2H_6	1.98	0.71	0.11
H_2(ref)	0.27	0.39	0.09

Table S8 Reactions analyzed for gas-phase ΔH comparison (at $25\,^{o}C$ and 101325 Pa).

Reaction #	Stoichiometry
0	$3H_2 + CO \rightarrow CH_4 + H_2O$
1	$5/2H_2 + CO \rightarrow 1/2C_2H_6 + H_2O$
2	$2H_2 + CO \rightarrow 1/2C_2H_4 + H_2O$
3	$1.5H_2 + CO \rightarrow 1/2C_2H_2 + H_2O$

Table S9 Reaction enthalpies (eV) of reactions (for RPBE gas-phase values) listed Table S8, are compared with the experimental reference values ΔH_{ref} , which are from NIST.[53]

Reaction #	ΔH_{ref} /eV	ΔH / eV	($\Delta H - \Delta H_{\text{ref}}$)/eV
0	-2.14	-2.20	-0.06
1	-1.8	-1.84	-0.04
2	-1.09	-1.14	-0.05
3	-0.19	-0.17	-0.02
Average of errors for reactions containing CO(g)			-0.04
Standard deviation of errors for reactions containing CO(g)			0.02

Table S10 OH binding energies in aqueous solution using three different DFT approaches, RPBE, RPBE-D3, and optB86b, compared with the OH_{ad} data in Figure 3a. The effects of the aqueous solvent on adsorption energies were treated via the VASPsol implicit solvation model.[20, 21]

	OH binding energy in solvation relative to Cu(111) (kJ/mol)				
	Cu(211)	Cu(110)	Cu(110)-rec	Cu(100)	Cu(111)
RPBE	38.7	15.5	27.6	11.0	0
RPBE-D3	38.3	14.3	25.3	16.3	0
optB86b	22.2	2.9	12.0	12.3	0

Table S11 CO binding energies in gas phase using three different DFT approaches, RPBE, RPBE-D3, and optB86b, compared with experimental CO TPD data in Figure 3b.

	CO binding energy in gas phase relative to Cu(111) (kJ/mol)				
	Cu(211)	Cu(110)	Cu(110)-rec	Cu(100)	Cu(111)
RPBE	69.9	63.2	62.5	57.7	50.9
RPBE-D3	96.1	95.0	86.3	91.4	75.4
optB86b	99.1	95.3	85.6	93.1	94.4
CO TPD (Figure 3b)	71.4	62.9	NA	56.1	49.1

Table S12 Comparison of free energies for *CO, *COH, *CHO, and *COCHO on four different facets, which are referenced to clean slab, with C atoms referenced to graphene, H atoms to 1/2 H_2, and O atoms to (H_2O-H_2).

	*CO (eV)		*COH (eV)		*CHO (eV)		*COCHO (eV)	
	RPBE	RBPE-D3	RPBE	RPBE-D3	RPBE	RPBE-D3	RPBE	RPBE-D3
Cu(211)	0.98	0.71	2.39	1.87	1.79	1.47	3.32	2.76
Cu(110)	1.04	0.72	2.56	2.20	1.81	1.31	3.18	2.42
Cu(110)-rec	1.06	0.84	2.66	2.34	1.83	1.47	3.26	2.67
Cu(100)	1.10	0.76	1.99	1.47	1.98	1.51	3.35	2.59
Cu(111)	1.16	0.90	2.33	2.00	2.12	1.68	3.79	2.93

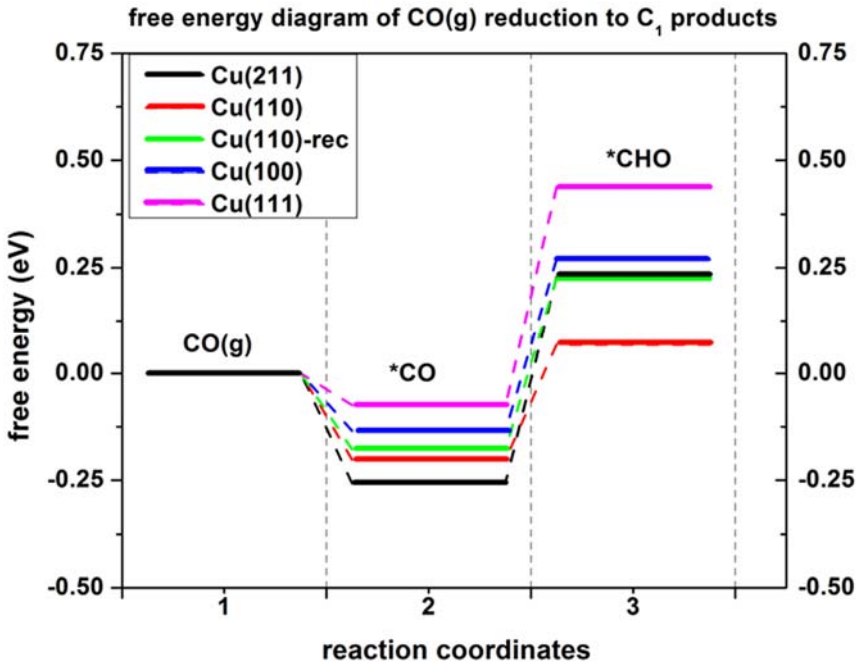

Figure S17. Free energy diagram for the *CHO pathway ($CO(g) \rightarrow *CO \rightarrow *CHO$) on five Cu facets, Cu(211), Cu(110), Cu(110)-rec, Cu(100) and Cu(111), at an applied potential of zero. Here, we use the RPBE adsorption energies for *CO and RPBE-D3 adsorption energies for *CHO.

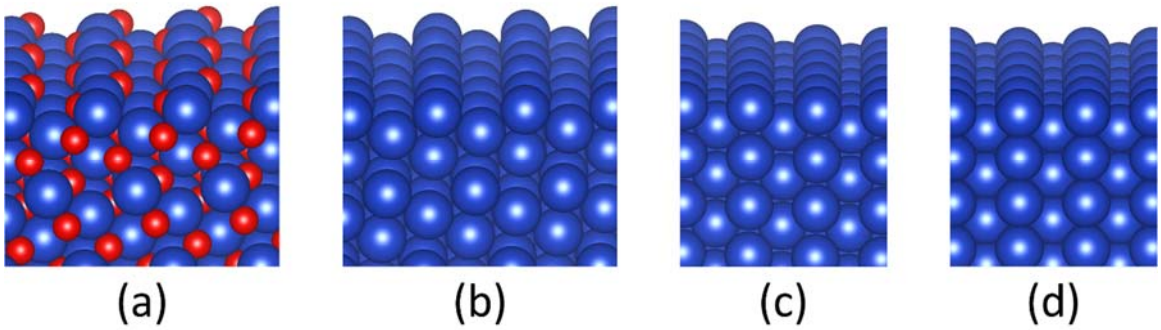

Figure S18. (a) The low-energy CuO(011) surface (b) The CuO(011) surface with oxygen atoms removed. (c) The CuO(011) surface with oxygen atoms removed and subsequent relaxation of atomic positions using density functional theory. (d) The high-energy Cu(110) surface. Blue and red spheres represent the Cu and Oxygen atoms, respectively.

S7. References

1. Raciti, D.; Livi, K. J.; Wang, C. *Nano Letters* **2015,** 15, 6829-6835.

2. Li, C. W.; Kanan, M. W. *J. Am. Chem. Soc.* **2012,** 134, 7231-7234.

3. Droog, J. M. M.; Schlenter, B. *Journal Of Electroanalytical Chemistry* **1980,** 112, 387-390.

4. Redhead, P. A. *Vacuum* **1962,** 12, 203-211.

5. Vollmer, S.; Witte, G.; Woll, C. *Catalysis Letters* **2001,** 77, 97-101.

6. Jiang, X.; Herricks, T.; Xia, Y. *Nano Lett.* **2002,** 2, 1333-1338.

7. Li, C. W.; Ciston, J.; Kanan, M. W. *Nature* **2014,** 508, 504-507.

8. Kohn, W.; Sham, L. J. *Phys. Rev.* **1965,** 140, A1133-A1138.

9. Kresse, G.; Furthmueller, J. *Phys. Rev. B* **1996,** 54, 11169-11186.

10. Kresse, G.; Furthmuller, J. *Comput. Mater. Sci.* **1996,** 6, 15-50.

11. Blöchl, P. E. *Phys. Rev. B* **1994,** 50, 17953-17979.

12. Perdew, J. P.; Burke, K.; Ernzerhof, M. *Phys. Rev. Lett.* **1996,** 77, 3865-3868.

13. Zhang, Y.; Yang, W. *Phys. Rev. Lett.* **1998,** 80, 890.

14. Grimme, S.; Antony, J.; Ehrlich, S.; Krieg, H. *J. Chem. Phys.* **2010,** 132, 154104/1-154104/19.

15. Sakong, S.; Groß, A. *ACS Catal.* **2016,** 6, 5575-5586.

16. Reckien, W.; Eggers, M.; Bredow, T. *Beilstein J. Org. Chem.* **2014,** 10, 1775-1784.

17. Sakong, S.; Naderian, M.; Mathew, K.; Hennig, R. G.; Groß, A. *J. Chem. Phys.* **2015,** 142, 234107/1-234107/12.

18. Tonigold, K.; Groß, A. *J. Comput. Chem.* **2012,** 33, 695-701.

19. Methfessel, M.; Paxton, A. T. *Phys. Rev. B* **1989,** 40, 3616-3621.

20. Mathew, K.; Sundararaman, R.; Letchworth-Weaver, K.; Arias, T. A.; Hennig, R. G. *J. Chem. Phys.* **2014,** 140, 084106/1-084106/8.

21. Mathew, K.; Hennig, R. G. *arXiv* **2016**, arXiv:1601.03346.

22. Wisesa, P.; McGill, K. A.; Mueller, T. *Phys. Rev. B* **2016,** 93, 155109/1-155109/10.

23. Norskov, J. K.; Rossmeisl, J.; Logadottir, A.; Lindqvist, L.; Kitchin, J. R.; Bligaard, T.; Jonsson, H. *J. Phys. Chem. B* **2004,** 108, 17886-17892.

24. Perdew, J. P.; Ruzsinszky, A.; Csonka, G. I.; Vydrov, O. A.; Scuseria, G. E.; Constantin, L. A.; Zhou, X.; Burke, K. *Phys. Rev. Lett.* **2008,** 100, 136406.

25. Stroppa, A.; Kresse, G. *New Journal of Physics* **2008,** 10, 063020.

26. Schimka, L.; Harl, J.; Stroppa, A.; Grüneis, A.; Marsman, M.; Mittendorfer, F.; Kresse, G. *Nat. Mater.* **2010,** 9, 741-744.

27. Fishman, M.; Zhuang, H. L.; Mathew, K.; Dirschka, W.; Hennig, R. G. *Phys. Rev. B* **2013,** 87, 245402/1-245402/7.

28. Dudarev, S. L.; Botton, G. A.; Savrasov, S. Y.; Humphreys, C. J.; Sutton, A. P. *Phys. Rev. B* **1998,** 57, 1505-1509.

29. Anisimov, V. I.; Zaanen, J.; Andersen, O. K. *Phys. Rev. B* **1991,** 44, 943-954.

30. Peterson, A. A.; Abild-Pedersen, F.; Studt, F.; Rossmeisl, J.; Norskov, J. K. *Energy Environ. Sci.* **2010,** 3, 1311-1315.

31. Blaylock, D. W.; Ogura, T.; Green, W. H.; Beran, G. J. O. *J. Phys. Chem. C* **2009,** 113, 4898-4908.

32. Liu, W.; Savara, A.; Ren, X.; Ludwig, W.; Dostert, K.-H.; Schauermann, S.; Tkatchenko, A.; Freund, H.-J.; Scheffler, M. *J. Phys. Chem. Lett.* **2012,** 3, 582-586.

33. Liu, W.; Tkatchenko, A.; Scheffler, M. *Acc. Chem. Res.* **2014,** 47, 3369-3377.

34. Błoński, P.; López, N. *J. Phys. Chem. C* **2012,** 116, 15484-15492.

35. Klimeš, J.; Bowler, D. R.; Michaelides, A. *Phys. Rev. B* **2011,** 83, 195131/1-195131/3.

36. Jiří, K.; David, R. B.; Angelos, M. *J. Phys.: Condens. Matter* **2010,** 22, 022201.

37. Román-Pérez, G.; Soler, J. M. *Phys. Rev. Lett.* **2009,** 103, 096102/1-096102/4.

38. Zhao, P.; He, Y.; Cao, D.-B.; Wen, X.; Xiang, H.; Li, Y.-W.; Wang, J.; Jiao, H. *Phys. Chem. Chem. Phys.* **2015,** 17, 19446-19456.

39. Hammer, B.; Hansen, L. B.; Nørskov, J. K. *Phys. Rev. B* **1999,** 59, 7413-7421.

40. Montoya, J. H.; Peterson, A. A.; Nørskov, J. K. *ChemCatChem* **2013,** 5, 737-742.

41. Shi, C.; Chan, K.; Yoo, J. S.; Nørskov, J. K. *Org. Process Res. Dev.* **2016,** 20, 1424-1430.

42. Li, Y.; Chan, S. H.; Sun, Q. *Nanoscale* **2015,** 7, 8663-8683.

43. Calle-Vallejo, F.; Koper, M. T. M. *Angew. Chem., Int. Ed.* **2013,** 52, 7282-7285.

44. Schouten, K. J. P.; Qin, Z.; Gallent, E. P.; Koper, M. T. M. *J. Am. Chem. Soc.* **2012,** 134, 9864-9867.

45. Schouten, K. J. P.; Pérez Gallent, E.; Koper, M. T. M. *ACS Catal.* **2013,** 3, 1292-1295.

46. Luo, W.; Nie, X.; Janik, M. J.; Asthagiri, A. *ACS Catal.* **2016,** 6, 219-229.

47. Montoya, J. H.; Shi, C.; Chan, K.; Nørskov, J. K. *J. Phys. Chem. Lett.* **2015,** 6, 2032-2037.

48. Xiao, H.; Cheng, T.; Goddard, W. A.; Sundararaman, R. *J. Am. Chem. Soc.* **2016,** 138, 483-486.

49. Durand, W. J.; Peterson, A. A.; Studt, F.; Abild-Pedersen, F.; Nørskov, J. K. *Surf. Sci.* **2011,** 605, 1354-1359.

50. Cheng, T.; Xiao, H.; Goddard, W. A. *J. Phys. Chem. Lett.* **2015,** 6, 4767-4773.

51. Tran, R.; Xu, Z.; Radhakrishnan, B.; Winston, D.; Sun, W.; Persson, K. A.; Ong, S. P. *Scientific Data* **2016,** 3, 160080.

52. Mishra, A. K.; Roldan, A.; de Leeuw, N. H. *J. Phys. Chem. C* **2016,** 120, 2198-2214.

53. Afeefy, H. Y.; Liebman, J. F.; Stein, S. E., Neutral Thermochemical Data. In *NIST Chemistry WebBook, NIST Standard Reference Database Number 69*, Linstrom, E. P. J.; Mallard, W. G., Eds. National Institute of Standards and Technology: Gaithersburg MD, USA, 2010.